# Molecular beam epitaxy of highly crystalline GeSnC using $CBr_4$ at low temperatures $\bigcirc$

Tuhin Dey <sup>(i)</sup>; Md. Shamim Reza <sup>(i)</sup>; Augustus Arbogast; Mark W. Holtz <sup>(i)</sup>; Ravi Droopad; Seth R. Bank <sup>(i)</sup>; Mark A. Wistey <sup>(i)</sup>



**☐** QBLOX

Appl. Phys. Lett. 121, 122104 (2022) https://doi.org/10.1063/5.0102093





CrossMark

Integrates all
Instrumentation + Software
for Control and Readout of
Superconducting Qubits
NV-Centers
Spin Qubits
NV-Centers Setup

# Molecular beam epitaxy of highly crystalline GeSnC using CBr<sub>4</sub> at low temperatures

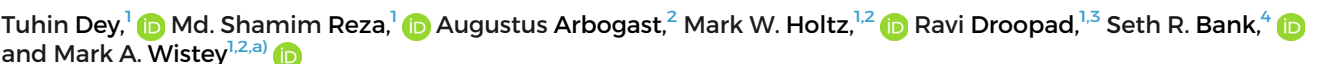
Cite as: Appl. Phys. Lett. **121**, 122104 (2022); doi: 10.1063/5.0102093 Submitted: 7 June 2022 · Accepted: 29 August 2022 · Published Online: 19 September 2022











### **AFFILIATIONS**

- <sup>1</sup>Materials Science, Engineering, and Commercialization Program, Texas State University, San Marcos, Texas 78666, USA
- <sup>2</sup>Department of Physics, Texas State University, San Marcos, Texas 78666, USA
- <sup>3</sup>Ingram School of Engineering, Texas State University, San Marcos, Texas 78666, USA
- $^4$ Microelectronics Research Center, University of Texas at Austin, Austin, Texas 78705, USA

#### **ABSTRACT**

Tensile-strained pseudomorphic  $Ge_{1-x-y}Sn_xC_y$  was grown on GaAs substrates by molecular beam epitaxy using carbon tetrabromide (CBr<sub>4</sub>) at low temperatures (171–258 °C). High resolution x-ray diffraction reveals good crystallinity in all samples. Atomic force microscopy showed atomically smooth surfaces with a maximum roughness of 1.9 nm. The presence of the 530.5 cm<sup>-1</sup> local vibrational mode of carbon in the Raman spectrum verifies substitutional C incorporation in  $Ge_{1-x-y}Sn_xC_y$  samples. X-ray photoelectron spectroscopy confirms carbon bonding with Sn and Ge without evidence of  $sp^2$  or  $sp^3$  carbon formation. The commonly observed Raman features corresponding to alternative carbon phases were not detected. Furthermore, no Sn droplets were visible in scanning electron microscopy, illustrating the synergy in C and Sn incorporation and the potential of  $Ge_{1-x-y}Sn_xC_y$  active regions for silicon-based lasers.

Published under an exclusive license by AIP Publishing. https://doi.org/10.1063/5.0102093

Si-based monolithic lasers are highly desired for full integration of electronic and photonic integrated circuits (EPICs). Due to their indirect bandgaps, group IV materials (C, Si, Ge, and Sn) are inefficient light emitters. However, a Ge conduction band at the  $\Gamma$  point is only 136 meV higher than the L point minimum, <sup>1</sup> making Ge a nearly direct bandgap. This has motivated research to modify the Ge band structure to create a direct bandgap. For example, tensile strained Ge lasers on Si have been demonstrated, albeit with prohibitively high threshold current densities  $(35 \, \text{kA/cm}^2)$ .

 ${\rm Ge_{1-x}Sn_x}$  becomes a direct-bandgap semiconductor with a value of x from 7% to 8%.<sup>3</sup> However, compressive strain in  ${\rm Ge_{1-x}Sn_x}$  pushes the bands back toward an indirect bandgap, necessitating even more  ${\rm Sn.^4}$  Double heterostructure  ${\rm Ge_{1-x}Sn_x}$  lasers have advanced markedly, and electrically injected lasers have been demonstrated but only at cryogenic temperatures.<sup>5,6</sup> Simultaneous achievement of electrical injection and room temperature operation has remained elusive for  ${\rm Ge_{1-x}Sn_x}$  lasers, motivating the search for alternative direct bandgap group IV active regions.

Ab initio modeling predicts that less than 1% C is necessary to create a direct bandgap in  $\mathrm{Ge_{1-y}C_y}^{7,8}$  and a strong direct transition makes  $\mathrm{Ge_{1-y}C_y}$  a promising active material for laser applications.

Unfortunately, segregation of disordered carbon, as seen using Raman spectroscopy,  $^{10}$  remains a challenge, and substitutional C was predicted to be energetically less favorable than non-substitutional C atoms.  $^{11,12}$  Despite these factors, we previously demonstrated growth of  $\mathrm{Ge_{1-y}C_y}$  using a specific C precursor to prevent C–C bonds with no defects seen in transmission electron microscopy (TEM).  $^{13}$ 

Growth of the ternary alloy  $Ge_{1-x-y}Sn_xC_y$  adds an additional control in epitaxial growth. The simultaneous incorporation of Sn and C into Ge is expected to make a direct bandgap at lower x and y mole fractions than their binary counterparts. The atomic radii ordering of Sn > Ge > C can partially compensate local strain and distortion of Ge. This promises a more stable material, similar to the improved optical properties of GaInNAs over GaNAs. Theoretical calculations predict that a Sn–C bond would be energetically favorable in the Ge lattice. Therefore, adding Sn might reduce C clustering, which would be a significant advance over previous attempts to grow  $Ge_{1-y}C_y$ . Furthermore, the addition of C to  $Ge_{1-x}Sn_x$  is expected to suppress Sn droplet formation. Therefore,  $Ge_{1-x-y}Sn_xC_y$  offers the best of both  $Ge_{1-y}C_y$  and  $Ge_{1-x}Sn_x$  while mitigating their respective growth challenges.

In this work, we investigate this hypothesis through the systematic study of  $Ge_{1-x-y}Sn_xC_y$  films synthesized using low-temperature

a) Author to whom correspondence should be addressed: mwistey@txstate.edu

molecular beam epitaxy (MBE). Materials were extensively characterized using high resolution x-ray diffraction (HR-XRD), Raman spectroscopy, atomic force microscopy (AFM), scanning electron microscopy (SEM), and x-ray photoelectron spectroscopy (XPS).

Ge<sub>1-x-v</sub>Sn<sub>x</sub>C<sub>v</sub> samples were grown on epi-ready GaAs (001) substrates in ultrahigh vacuum ( $\sim 1 \times 10^{-9}$  Torr) MBE with Ge and Sn solid source effusion cells, and commercially available, high-purity carbon tetrabromide (CBr<sub>4</sub>) for C. CBr<sub>4</sub> is a well-known dopant source for III-V epitaxy, 18 which delivers single C atoms to the surface rather than the C clusters from commonly used sources such as graphite. 17,19 Substrate temperatures (T<sub>sub</sub>) were calibrated using indium droplet melting and KSA BandiT sensor. Atomic hydrogen was used to desorb the native oxide and remove surface hydrocarbons at 404°C. Reflection high-energy electron diffraction (RHEED) showed a bright  $2 \times 4$  reconstruction pattern after deoxidation. An initial 150 nm thick buffer layer of Ge was grown at 431 °C to produce a uniform, flat surface, confirmed by RHEED and AFM (roughness = 0.1 nm). The Ge<sub>1-x-y</sub>Sn<sub>x</sub>C<sub>y</sub> samples were then grown at low temperatures (171-258 °C) to minimize Sn segregation and to maximize Sn and C incorporation. The nominal thickness of Ge<sub>1-x-y</sub>Sn<sub>x</sub>C<sub>y</sub> was 180 nm for all samples to avoid strain relaxation, see the supplementary material for additional information.

The growth process was monitored in real time by *in situ* RHEED.  $Ge_{1-x-y}Sn_xC_y$  layers grown at lower temperatures showed streaky  $2 \times$  RHEED patterns, as shown in Figs. 1(a)-1(d). The fundamental and half-order diffraction lines were intense and equidistant. With increasing substrate temperature, half-order diffraction intensities decreased, and fundamental diffraction lines modulated. These effects indicate decreasing average terrace sizes. At a growth temperature of 258 °C, the half-order streaks completely disappeared and RHEED patterns became spotty, indicating conversion to a 3D island growth mode, Fig. 1(e).

Surface morphology was investigated by *ex situ* AFM (Bruker Dimension) in a tapping mode using Si probes (tip radius 8 nm, force

constant 5 N/m). The AFM shows very flat surfaces for all samples grown at low temperatures, Figs. 1(a)–1(d). At  $T_{sub}=258\,^{\circ}C$ , the surface became rough with height amplitude 18 nm, although overall root mean square (rms) roughness remained low, 1.9 nm, Fig. 1(e). Detailed  $2\times 2~\mu\text{m}^2$  scans are shown in Fig. 1; rms roughness values in Table I are from  $10\times 10~\mu\text{m}^2$  scan area of the same position.

HR-XRD (Rigaku SmartLab) and reciprocal space mapping (RSM) were performed with a Cu Ka1 source with a Ge (220) monochromator. Results are shown in Fig. 2. The 2Theta-Omega scans around the (004) diffraction conditions are shown in Fig. 2(a). Well-defined diffractions at 66.04° and 65.94° are from the GaAs substrate and the Ge buffer layer, respectively. The sharp  $\text{Ge}_{1-x-y}\text{Sn}_x\text{C}_y$  diffractions at higher angles confirm incorporation of substitutional Sn and C in the alloy with smaller out-of-plane lattice constants  $(a_\perp)$ . Pendellösung fringes are consistent in all samples with the presence of abrupt and flat interfaces. The narrow FWHM in HR-XRD rocking curves confirms good crystal quality with uniform epitaxial layers.

RSM was performed around the asymmetric (115) reflection, shown in Fig. 2(b) for the sample grown at  $T_{sub}=171\,^{\circ}\mathrm{C}$  to evaluate the degree of relaxation. The GaAs substrate, Ge buffer, and  $Ge_{1-x-y}Sn_xC_y$  film peaks have the same  $Q_x$  position, signifying the in-plane lattice spacing is matched to that of the substrate without relaxation. The different  $Q_z$  values observed confirm different lattice constants in the perpendicular growth direction. We obtain out-of-plane lattice constant  $a_{\perp}=5.624\,\text{Å}$  for  $Ge_{1-x-y}Sn_xC_y$  grown at  $T_{sub}=171\,^{\circ}\mathrm{C}$ . The lattice constant is in good agreement with result from the 2Theta-Omega diffraction measurement.

The  $Ge_{1-x-y}Sn_xC_y$  is pseudomorphically strained to the substrate, leaving  $a_\perp$  as the sole independent measured parameter. This prevents simultaneously determining both x and y in the  $Ge_{1-x-y}Sn_xC_y$  ternary alloy from HR-XRD, since each will affect the lattice constant. Therefore, a set of C-free  $Ge_{1-x}Sn_x$  samples were grown at the same series of temperatures under identical conditions. The 2Theta-Omega measurements show a decreasing trend of %Sn with increasing

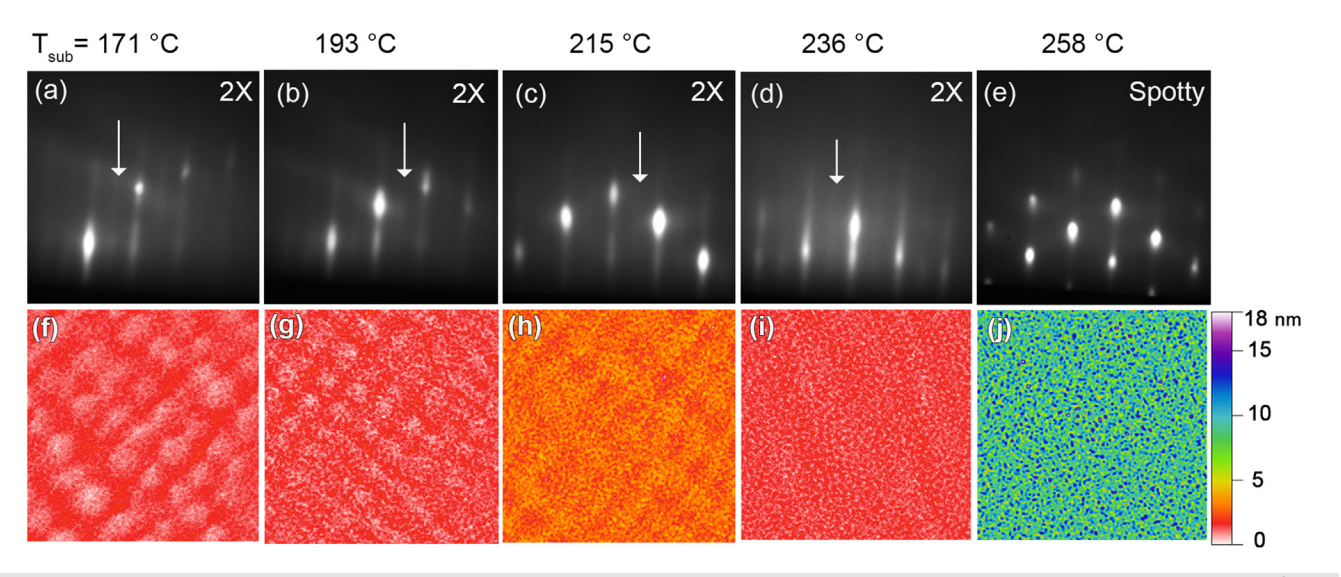


**FIG. 1.** (a)–(d) RHEED shows  $2\times$  surface reconstruction (shown by arrow) for  $T_{sub}=171-236\,^{\circ}C$ . (e) RHEED shows 3D spots at  $258\,^{\circ}C$ . (f)–(i) AFM scans  $2\times2~\mu\text{m}^2$  show flat surfaces for  $T_{sub}=171-236\,^{\circ}C$ . The rms roughness (Rq) from  $10\times10~\mu\text{m}^2$  scans are presented in Table I. (j) Sample grown at  $258\,^{\circ}C$  shows a maximum feature of  $18\,\text{nm}$  with Rq =  $1.9\,\text{nm}$ .

236

258

0.2

1.9

0.5%

0.4%

XRD FWHM Substrate Equivalent Ge<sub>1-x</sub>Sn<sub>x</sub> %C Out-of-plane In-plane AFM rms temperature (°C) growths %Sn (subst.) strain  $(\varepsilon_{\perp})$ strain  $(\varepsilon_{\parallel})$ (arc-sec) roughness (nm) 171 3.9 -0.17%1.1% 42.5 0.3 2.6 193 2.7 2.1 -0.17%1.1% 42.9 0.4215 2.6 2.0 -0.16%1.0% 49.1 0.3

-0.08%

-0.06%

TABLE I. Summary of Ge<sub>1-x-v</sub>Sn<sub>x</sub>C<sub>v</sub> characterization results assuming %Sn from equivalent Ge<sub>1-x</sub>Sn<sub>x</sub> growths.

1.6

1.2

temperatures in these samples due to Sn segregation. Assuming similar Sn incorporation in  $Ge_{1-x-y}Sn_xC_y$ , C concentrations were subsequently obtained from  $a_\perp$ . The results are summarized in Table I.

2.4

2.0

The out-of-plane strain in the film  $\varepsilon_{\perp}=(a_{\perp}-a_0)/a_0$  was calculated using  $a_{\perp}$  from the  $Ge_{1-x-y}Sn_xC_y$  (004) peak positions in the 2Theta-Omega scans and assuming Vegard's law for the unstrained  $Ge_{1-x-y}Sn_xC_y$  lattice constants  $(a_0)$ . The fully relaxed (R=1) position of the  $Ge_{1-x-y}Sn_xC_y$  sample at  $T_{sub}=171\,^{\circ}C$  is indicated by a blue dashed line in Fig. 2(a); for all samples, a slight up-shift of peak position is observed that diminishes with higher  $T_{sub}$ . The up-shift indicates the presence of tensile residual in-plane strain  $(\varepsilon_{\parallel})$ , assuming  $\varepsilon_{\parallel}=-C_{11}/(2C_{12})\,\varepsilon_{\perp}$  and published elastic constants. The results are summarized in Table I.

The decreasing trend observed for in-plane strain with increasing  $T_{sub}$  may be interpreted based on two factors. First is carbon clustering. D'Arcy-Gall *et al.* reported that carbon occupying a single site in the Ge lattice is less stable than defects with two and three C atoms occupying the same lattice site (C cluster), <sup>12</sup> meaning that the carbon may occupy both substitutional and non-substitutional sites in the Ge lattice under ordinary growth conditions. Therefore, the total C concentration (*y*) will be composed of substitutional carbon ( $y_{sub}$ ) and clusters ( $y_{cluster}$ ). The Ge–C split interstitials also described for  $Ge_{1-y}C_y$  alloys prepared by a sputtering process is not expected to be present in

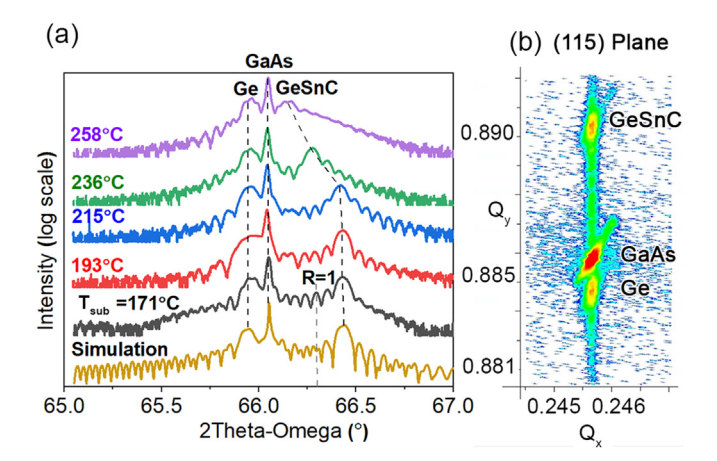


**FIG. 2.** (a) HR-XRD 2Theta-Omega scans about GaAs (004) as a function of  $T_{\text{sub}} = 171-258\,^{\circ}\text{C}$ . Relaxed position for the sample at 171 $\,^{\circ}\text{C}$  is indicated by R = 1. Simulation based on Sn = 3.9%, C = 2.6%, (b) RSM around the (115) plane for the sample at 171 $\,^{\circ}\text{C}$ . Vertical alignment shows the buffer and the epi-layer are coherent with the substrate without strain relaxation.

our MBE grown samples.  $^{17}$  It is noteworthy that substitutional carbon induces tensile local strain in Ge, while non-substitutional carbon induces compressive strain.  $^{12}$  Therefore, it may be possible that at higher  $T_{\rm sub}$  of  $236\,^{\circ}\text{C}$  and  $258\,^{\circ}\text{C}$ , more carbon resides in non-substitutional sites than substitutional sites, reducing tensile strain.

55.9

49.4

A second possible explanation for the trend in Fig. 2(a) is that Sn is expected to make carbon incorporation more favorable. Therefore, loss of Sn due to segregation at higher growth temperatures might lead to an even faster decrease in the substitutional C content and decreasing tensile strain. However, this explanation seems unlikely since none of our  $Ge_{1-x-y}Sn_xC_y$  samples show evidence of Sn segregation.

Unpolarized Raman measurements (Horiba LabRam) were performed with spectral resolution  $<\!0.5\,\mathrm{cm^{-1}}$  using 632.8 nm laser excitation ( $<\!10$  mW). Light at this wavelength has an optical penetration depth of 30 nm in Ge,  $^{21}$  so the Raman measurements probe the alloy layers without contribution from the underlying substrate. Spectra are seen in Fig. 3(a) for both  $\mathrm{Ge_{1-x-y}Sn_xC_y}$ ,  $\mathrm{Ge_{1-x}Sn_x}$  as a control and Ge buffer. The dominant peak at 300 cm $^{-1}$  corresponds to the first-order allowed Ge–Ge vibration. Based on fits of the data using Lorentzian line shapes, this band ranges in energy between 300.0 and 300.5 cm $^{-1}$  for these samples and exhibits a narrow linewidth  $< 3.5\,\mathrm{cm}^{-1}$ , confirming excellent crystal quality of the alloy. All intensities are normalized to the dominant Ge–Ge band. The second-order Raman peaks, denoted SO<sub>Ge</sub>, are also present in Raman measurements of Ge as previously reported.  $^{22}$ 

In Fig. 3(a), we see prominent peaks at  $\sim$ 188 cm<sup>-1</sup> and 263 cm<sup>-1</sup> in the C-free  $Ge_{1-x}Sn_x$  sample, attributed to the Sn-Sn and Ge-Sn vibrational modes, respectively.<sup>23,24</sup> The Sn-Sn peak broadens in Ge<sub>1-x-v</sub>Sn<sub>x</sub>C<sub>v</sub> samples, an effect that is attributable to different local Sn surroundings at low concentrations and to mix with the non-zonecenter phonons in these alloys. This Sn-Sn mode is band-resonant and described as an admixture of the Sn-Sn vibration and Ge phonons.<sup>23</sup> In addition, D'Costa et al. discussed that the broad Sn-Sn band cannot be interpreted as a phonon in  $\alpha$ -Sn,<sup>24</sup> and the weak Sn-Sn features we see here rule out significant Sn segregation upon addition of carbon. The feature at 285 cm<sup>-1</sup> has been attributed to disorder-activated scattering by non-zone-center phonons in Ge,<sup>22</sup> denoted DA<sub>Ge</sub> in Fig. 3(b). Furthermore, the Ge-Sn band is not resolved in the  $\text{Ge}_{1\text{--}x\text{--}y}\text{Sn}_x\text{C}_y$  samples, although a shoulder is present just above 270 cm<sup>-1</sup> as seen in Fig. 3(b). Therefore, it appears that the Ge-Sn peak slightly broadens and blueshifts to merge with the DA<sub>Ge</sub> feature upon the addition of carbon.

Also seen in the Raman spectra for the ternary  $Ge_{1-x-y}Sn_xC_y$  samples, but absent in  $Ge_{1-x}Sn_x$  and Ge, is a narrow peak at 530.5 cm<sup>-1</sup> in Fig. 3(a) and expanded in 3(c). This narrow feature has

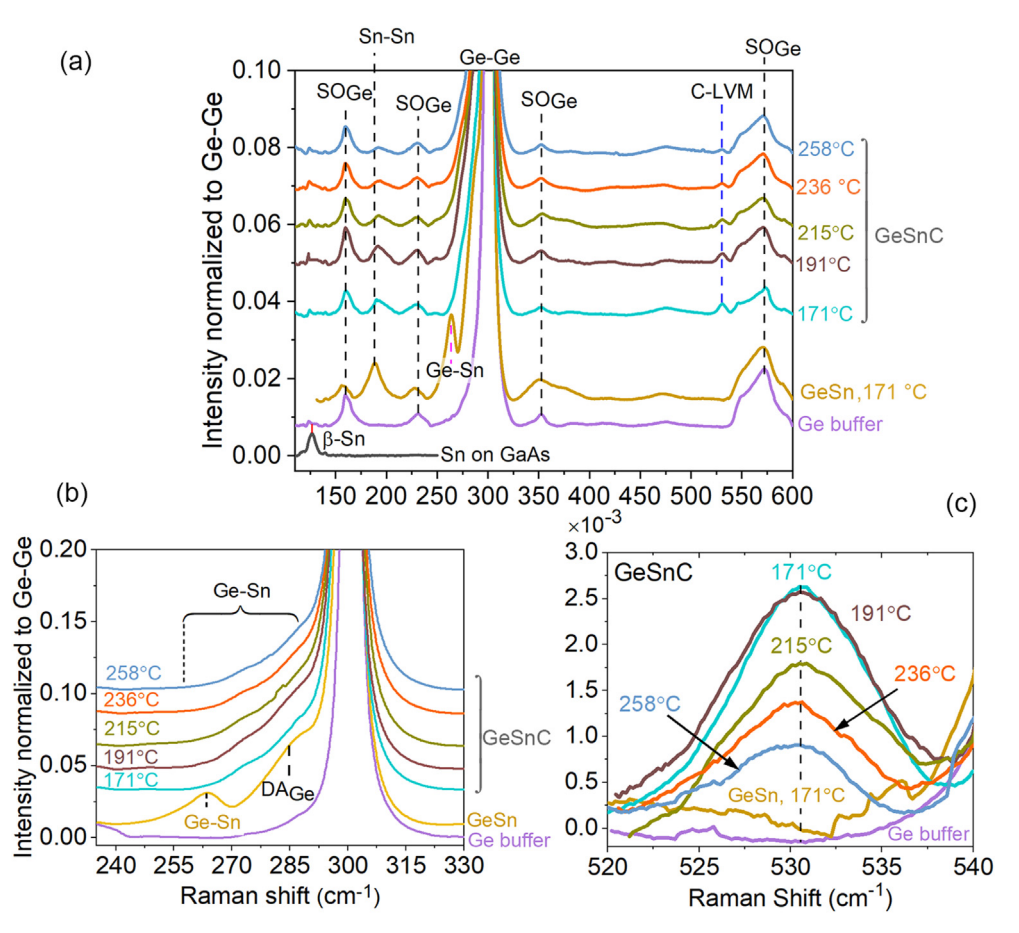


**FIG. 3.** (a) Raman spectra of  $Ge_{1-x}Sn_x$ . Ge buffer, and  $Ge_{1-x-y}Sn_xC_y$  for series of  $T_{sub}$ . (b)  $Ge_{1-x}Sn_x$  shows distinct peak at 263 cm<sup>-1</sup>, and  $Ge_{1-x-y}Sn_xC_y$  shows broad shoulder in the range of 270–285 cm<sup>-1</sup> for the Ge–Sn mode. (c) C-LVM mode at 530.5 cm<sup>-1</sup>.

been previously reported in  $Ge_{1-y}C_y$  and is attributed to the local vibrational mode (LVM) of substitutional carbon. <sup>23</sup> Observation of the carbon local mode is significant, because it directly confirms the presence of substitutional C. The intensity of the Ge–C local mode is very low compared with the Ge–Ge mode. This is expected from the low concentration of carbon. Based on fits to the data, the C-LVM is found to be narrow with FWHM  $\sim 10~{\rm cm}^{-1}$ . We also note that the relative intensity of the C-LVM decreases at higher  $T_{\rm sub}$ , as shown in Fig. 3(c). Ternary alloys present a variety of possible local environments near the C atom. Examples include nearest-neighbor tetrahedral sites that are composed of Ge and one or more Sn atoms, plus a large variety of second-nearest-neighbor possibilities. However, with the exception of C–C bonding, diverse local atomic arrangements, such as C–Ge vs C–Sn bonds, are not expected to strongly affect the C-LVM frequency due to the light mass of C compared with the other atoms.

Stable  $\beta$ -Sn exhibits a Raman band at 126 cm<sup>-1</sup>, as shown in Fig. 3(a) for Sn deposited on GaAs. In examining the GeSnC alloys in this range, we see very weak features at 123 cm<sup>-1</sup>. This weak feature is also present in the Ge reference spectrum, although not observed in bulk Si. Although we do not have a definitive assignment, we attribute this weak feature to higher-order scattering from Ge.  $\beta$ -Sn is not observed

in (2°) grazing angle XRD at  $2\theta = 30-32^{\circ}$ ; see the supplementary material. These exclude the presence of  $\beta$ -Sn in our GeSnC samples.

Raman spectra were collected from the 1300 to  $1600\,\mathrm{cm}^{-1}$  range to check for the presence of  $\mathrm{sp}^2$ - or  $\mathrm{sp}^3$ -like amorphous carbon, as previously reported for  $\mathrm{Ge}_{1-y}\mathrm{C}_y$  samples grown by sputtering or arc plasma. <sup>10</sup> Our data show no Raman features in this range even at low relative intensity ( $\sim 10^{-4}$ ) to the Ge–Ge bands in  $\mathrm{Ge}_{1-x-y}\mathrm{Sn}_x\mathrm{C}_y$  samples.

XPS measurements were performed using a monochromated Al K $\alpha$  (1486.6 eV) x-ray source with an energy resolution of  $\leq$ 0.5 eV to investigate the chemical bonding state of C and Sn in the sample grown at 215 °C. *In situ* Ar ion etching was performed for 20 s to remove surface contamination and oxides. The sample charging was neutralized using an electron flood gun. Before the etching, surface contamination showed an adventitious C1s peak at 284.8 eV. After etching, the C–C peak disappeared entirely, and a peak at 283.24 eV appeared which can be deconvoluted into peaks at 283.1 and 283.8 eV as shown in Fig. 4(a). We expect C–Sn would have a lower binding energy than C–Ge since Sn is less electronegative than Ge. Therefore, we ascribe the bands in Fig. 4(a) at 283.1 eV to C–Sn bonds and 283.8 eV to C–Ge bonds. <sup>25</sup> The latter peak is a well-established metal

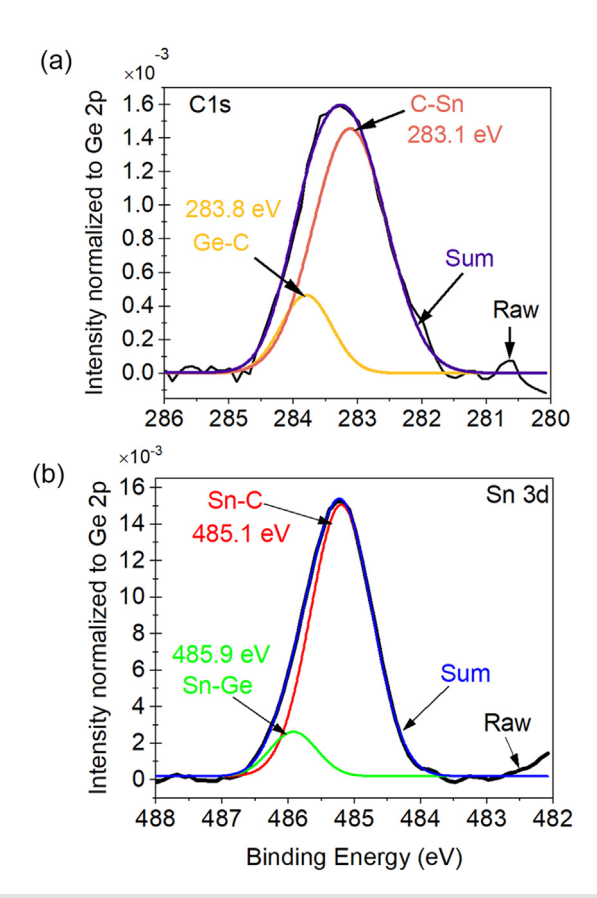


**FIG. 4.** The XPS C1s and Sn 3d core energy spectra for the sample at  $T_{sub}$ =223 °C. (a) C1s fitted with two Gaussian peaks, at 283.1 eV for C–Sn and 283.8 eV for Ge–C.(b) Sn 3d fitted with two Gaussian peaks, at 485.1 eV for Sn–C and 485.9 eV for Sn–Ge

carbide XPS feature for Ge–C. The FWHM for the C–Sn and C–Ge peaks are 0.9 and 1.3 eV, respectively. Attempts to fit two additional peaks at 284.3 and 285.3 eV for sp<sup>2</sup> and sp<sup>3</sup> C bonds<sup>26</sup> failed. This further confirms the sample is free from high concentration of segregated carbon.

We also observed a Sn 3d peak that appears to be the convolution of two different peaks, which we tentatively assign as 485.1 eV (Sn–C) and 485.9 eV (Sn–Ge) in Fig. 4(b). The positive shift of binding energy compared with the Sn–Sn metal peak at 484.9 eV signifies Sn is bonding with either C or Ge. A preliminary attempt to quantify the atomic percentage using XPS suggests less C (1.2  $\pm$  0.6%) and Sn (1.8  $\pm$  0.6%) compared with XRD estimates (C = 2.6%, Sn = 2%) for the sample grown at 215 °C. Note that these results are close to the measurement limit of our XPS, contributing to uncertainty.

Figure 5 shows SEM images of  $Ge_{1-x}Sn_x$  and  $Ge_{1-x-y}Sn_xC_y$  grown under identical conditions at  $T_{sub} = 258\,^{\circ}C$ . Three types of domains are identified in  $Ge_{1-x}Sn_x$  as reported in Ref. 27. A corresponds to Sn rich nanoparticles, confirmed by energy-dispersive x-ray spectroscopy (EDS), B to trenches formed by surface movement of Sn-rich droplets, and C is the  $Ge_{1-x}Sn_x$  surface. In contrast, no droplets or trenches are seen for the  $Ge_{1-x-y}Sn_xC_y$  sample, see Fig. 5(b).

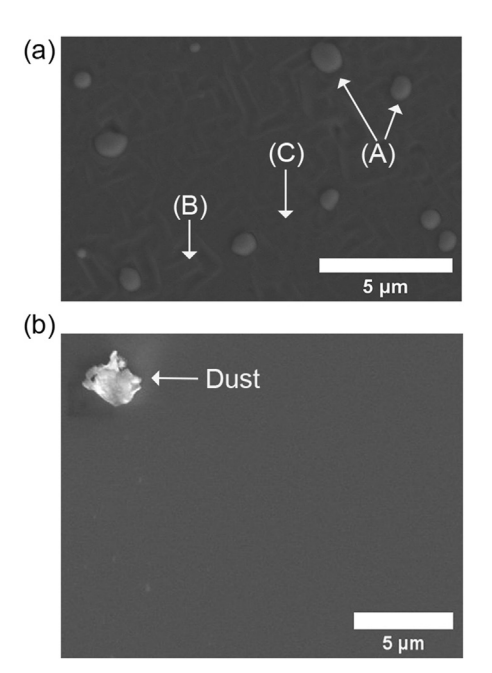


**FIG. 5.** (a) SEM shows Sn droplets, trenches, and GeSn surfaces in the  $Ge_{1-x}Sn_x$  sample. (b)  $Ge_{1-x-y}Sn_xC_y$  sample shows no such features. NB: Particle included for focus in the GeSnC surface.

We attribute the dramatic increase in material quality to be the result of Sn and C compensating each other's local strain and distortion of the surface during growth. <sup>28</sup> This is supported by our *ab initio* calculations similar to Ref. 9. When replacing a single Ge atom with C, its four nearest Ge neighbors contract 0.36 Å from their original positions toward C. The resulting C–Ge bonds are 14.8% shorter than the native Ge–Ge bond (2.090 vs 2.45 Å), but not as short as a "natural" C–Ge bond (2.000 Å) due to the surrounding Ge lattice rigidity. Similarly, an isolated Sn atom in Ge pushes its four neighbors each outward by 0.127 Å. The resulting Sn–Ge bond length (2.575 Å) is 6.6% longer than that of Ge–Ge, but the native bond length would be 14% longer (2.854 Å) without the surrounding rigid lattice. When the C and Sn atoms are bonded directly to each other, the displacement of each neighboring Ge atom from its ideal lattice position is reduced to 0.069 Å.

In summary, we have presented the epitaxial growth of tensile strained  $Ge_{1-x-y}Sn_xC_y$  layers using commercially available  $CBr_4$  as a carbon precursor. HR-XRD shows all layers are pseudomorphic to the GaAs substrate with high crystal quality. Raman spectroscopy verifies substitutional C incorporation in Ge without alternate C or Sn phases. XPS shows C–Sn and C–Ge bonds without any C–C defects. AFM measurements show the sample with highest Sn and C concentration to have an atomically flat surface. SEM reveals no surface Sn droplets on the  $Ge_{1-x-y}Sn_xC_y$  surface, which we attribute to local strain compensation of Sn by C. This approach offers an opportunity for high quality crystal growth of direct bandgap group IV alloys for silicon photonics.

See the supplementary material for additional information on growth conditions, XRD grazing angle measurements, and substrate temperature calibration.

The authors acknowledge support from the National Science Foundation under Grant Nos. DMR-1508646, CBET-1438608, and PREM DMR-2122041, the Center for Dynamics and Control of Materials is supported by the National Science Foundation under Award No. DMR-1720595, and additional support by the University of Texas at Austin. The authors also thank Casey Smith for instrumentation technical support, and S. R. Rab and A. Siddique for XRD discussions.

# **AUTHOR DECLARATIONS Conflict of Interest**

The authors have no conflicts to disclose.

# **Author Contributions**

Tuhin Dey: Conceptualization (equal); Data curation (lead); Formal analysis (equal); Investigation (equal); Methodology (equal); Validation (equal); Visualization (lead); Writing – original draft (lead); Writing - review & editing (equal). Md. Shamim Reza: Formal analysis (supporting); Resources (equal). Augustus Arbogast: Formal analysis (supporting); Resources (equal); Writing - review & editing (supporting). Mark W. Holtz: Formal analysis (equal); Funding acquisition (supporting); Investigation (equal); Methodology (equal); Resources (supporting); Supervision (equal); Validation (equal); Writing - review & editing (equal). Ravi Droopad: Resources (equal); Validation (supporting). Seth R. Bank: Resources (supporting); Writing - review & editing (equal). Mark A. Wistey: Conceptualization (equal); Formal analysis (equal); Funding acquisition (lead); Investigation (equal); Methodology (equal); Project administration (equal); Resources (lead); Software (lead); Supervision (lead); Validation (equal); Visualization (equal); Writing - review & editing (lead).

## DATA AVAILABILITY

The data that support the findings of this study are available from the corresponding author upon reasonable request.

# REFERENCES

- <sup>1</sup>Physics of Group IV Elements and III-V Compounds, edited by O. Madelung, Landolt-Börnstein: Numerical Data and Functional Relationships in Science and Technology (Springer, Berlin, 1982).
- <sup>2</sup>J. F. Liu, X. C. Sun, R. Camacho-Aguilera, L. C. Kimerling, and J. Michel, Opt. Lett. 35(5), 679 (2010).
- <sup>3</sup>R. Chen, H. Lin, Y. Huo, C. Hitzman, T. I. Kamins, and J. S. Harris, Appl. Phys. Lett. 99(18), 181125 (2011).

- <sup>4</sup>S. Gupta, B. Magyari-Köpe, Y. Nishi, and K. C. Saraswat, J. Appl. Phys. 113(7), 073707 (2013).
- <sup>5</sup>Y. Zhou, S. Ojo, C.-W. Wu, Y. Miao, H. Tran, J. M. Grant, G. Abernathy, S. Amoah, J. Bass, G. Salamo, W. Du, G.-E. Chang, J. Liu, J. Margetis, J. Tolle, Y.-H. Zhang, G. Sun, R. A. Soref, B. Li, and S.-Q. Yu, Photonics Res. 10(1), 222
- <sup>6</sup>Y. Zhou, Y. Miao, S. Ojo, H. Tran, G. Abernathy, J. M. Grant, S. Amoah, G. Salamo, W. Du, J. Liu, J. Margetis, J. Tolle, Y-h Zhang, G. Sun, R. A. Soref, B. Li, and S.-Q. Yu, Optica 7(8), 924 (2020).
- <sup>7</sup>C. A. Stephenson, W. A. O'brien, M. Qi, M. Penninger, W. F. Schneider, and M. A. Wistey, J. Electron. Mater. 45(4), 2121 (2016).
- <sup>8</sup>C. A. Stephenson, W. A. O'Brien, M. W. Penninger, W. F. Schneider, M. Gillett-Kunnath, J. Zajicek, K. M. Yu, R. Kudrawiec, R. A. Stillwell, and M. A. Wistey, J. Appl. Phys. 120(5), 053102 (2016).
- <sup>9</sup>I. A. Gulyas, C. A. Stephenson, Q. Meng, S. R. Bank, and M. A. Wistey, J. Appl. Phys. 129(5), 055701 (2021).
- <sup>10</sup>M. Okinaka, Y. Hamana, T. Tokuda, J. Ohta, and M. Nunoshita, J. Cryst. Growth 249, 78 (2003).
- <sup>11</sup>J. D'Arcy-Gall, P. Desjardins, I. Petrov, J. E. Greene, J. E. Paultre, R. A. Masut, S. C. Gujrathi, and S. Roorda, J. Appl. Phys. 88(1), 96 (2000).
- <sup>12</sup>J. D'Arcy-Gall, D. Gall, I. Petrov, P. Desjardins, and J. E. Greene, J. Appl. Phys. 90(8), 3910 (2001).
- <sup>13</sup>C. Stephenson, M. Gillett-Kunnath, W. O'Brien, R. Kudrawiec, and M. Wistey, Crystals 6(12), 159 (2016).
- <sup>14</sup>V. Lordi, H. B. Yuen, S. R. Bank, M. A. Wistey, J. S. Harris, and S. Friedrich, Phys. Rev. B 71(12), 125309 (2005).
- <sup>15</sup>A. Chroneos, Phys. Status Solidi B **244**(9), 3206 (2007).
- 16 E. Kamiyama, K. Sueoka, K. Terasawa, T. Yamaha, O. Nakatsuka, S. Zaima, K. Izunome, K. Kashima, and H. Uchida, Thin Solid Films 592, 54 (2015).
- 17 S. Y. Park, J. D'Arcy-Gall, D. Gall, Y. W. Kim, P. Desjardins, and J. E. Greene, J. Appl. Phys. 91(6), 3644 (2002).
- <sup>18</sup>S. Godey, S. Dhellemmes, A. Wilk, M. Zaknoune, and F. Mollot, J. Cryst. Growth 278(1), 600 (2005).
- <sup>19</sup>K. J. Roe, M. W. Dashiell, J. Kolodzey, P. Boucaud, and J. M. Lourtioz, J. Vacuum Sci. Technol. B: Microelectron. Nanometer Struct. Process., Meas., Phenom. 17(3), 1301 (1999).
- <sup>20</sup>H. H. Thylén Radamson, "Moore's law for photonics and electronics," in Monolithic Nanoscale Photonics-Electronics Integration in Silicon and Other Group IV Elements (Cambridge, MA, 2015), Chap. 4.
- <sup>21</sup>D. E. Aspnes and A. A. Studna, Phys. Rev. B 27(2), 985 (1983).
- <sup>22</sup>B. A. Weinstein and M. Cardona, Phys. Rev. B 7(6), 2545 (1973).
- <sup>23</sup>W. H. Weber, B. K. Yang, and M. Krishnamurthy, Appl. Phys. Lett. **73**(5), 626 (1998).
- <sup>24</sup>V. R. D'Costa, J. Tolle, R. Roucka, C. D. Poweleit, J. Kouvetakis, and J. Menéndez, Solid State Commun. 144(5-6), 240 (2007).
- 25 T. Bruce, I. Bello, L. J. Huang, W. M. Lau, M. High, V. Strnad, and P. Panchhi, J. Appl. Phys. 76(1), 552 (1994).
- <sup>26</sup>S.-E. Ong, S. Zhang, H. Du, and D. Sun, Diamond Related Mater. **16**(8), 1628
- <sup>27</sup>T. Tsukamoto, N. Hirose, A. Kasamatsu, T. Mimura, T. Matsui, and Y. Suda, Appl. Phys. Lett. 106(5), 052103 (2015).
- <sup>28</sup>R. Matsutani, K. Sueoka, and E. Kamiyama, Phys. Status Solidi C 11(11-12),
- 1718 (2014).